Fast, furious, and gassy: Etna's explosive eruption from the mantle

Anna Barth, Maxim Portnyagin, Nikita Mironov, Francois Holtz, Yves Moussallam, Estelle F. Rose-Koga, Daniel Rasmussen, Henry Towbin, Helge Gonnermann, Euan J.F. Mutch, et al.

- Magma in Etna's Fall Stratified eruption was extremely volatile-rich (9600 ppm CO_2)
- Magma ascended from storage at the Moho to the surface in <1-5 days
- High volatiles and fast ascent likely caused explosive intensity of this picritic magma

Fast, furious, and gassy: Etna's Explosive Eruption from the Mantle

Anna Barth, Maxim Portnyagin, Nikita Mironov, Francois Holtz, Yves Moussallam, Estelle F. Rose-Koga, Daniel Rasmussen, Henry Towbin, Helge Gonnermann, Euan J. F. Mutch, Silvio Rotolo,Terry Plank

Abstract

The 3930 BP Fall Stratified (FS) eruption at Mt. Etna is a rare example of a highly explosive eruption of primitive (picritic) magma directly from the mantle. The eruption produced ash plumes up to an estimated 20 km height, leading to a volcanic explosivity index (VEI) 4 (subplinian). Given its volatile-rich and primitive nature, the FS magma may have ascended rapidly from great depths to avoid fractionation and mixing within the extensive plumbing system beneath Etna. To determine the pressures from which the FS magma derived, we perform rehomogenization experiments on melt inclusions hosted in Fo_{90-91} olivines to resorb shrinkage bubbles and determine the initial H_2O and CO_2 in the melt. With measured CO_2 concentrations of up to 9600 ppm, volatile solubility models yield magma storage pressures of 630–800 MPa. These correspond to depths of 24–30 km, which are comparable to the seismologically estimated Moho. Therefore, the magma's high CO_2 concentration must come from carbon in the mantle (likely from subducted carbonates), as opposed to assimilation of shallow (<10 km) crustal carbonates.

Diffusion modeling of H_2O and forsterite zonation profiles in clear, euhedral, and crystallographically oriented olivines indicates rapid ascent of magma directly from its source region to the surface. Forsterite profiles exhibit a narrow rim of growth zoning but no detectable diffusional zoning, reflecting maximum ascent times of 1–5 days. Eighteen measured H_2O profiles result in remarkably uniform decompression rates of 0.47 MPa/s (95% confidence interval of 0.16–1.28 MPa/s), which is among the fastest measured for basaltic-intermediate magmas. These decompression rates indicate that the final stage of magma ascent over the region in which H_2O degasses (between the surface and ~ 15 km)

occurred extremely fast at ~ 17.5 m/s. This eruption may provide a link between primary magma composition and eruption intensity: we propose that the unusually explosive nature of this picritic eruption was driven by high H_2O and CO_2 concentrations, which led to continuously rapid ascent without stalling, all the way from the Moho.

1. Introduction

Basaltic volcanism occurs over a vast range of scales and styles, from effusive lava flows, to Strombolian, Hawaiian, and up to Plinian eruption styles (Houghton & Gonnermann, 2008). Etna is a prime example of a volcano which hosts all of these eruption styles (Branca & Del Carlo, 2005; Coltelli et al., 1998; Zuccarello et al., 2022). The controls on eruption intensity remains poorly understood, especially for subplinian and plinian eruptions (Houghton & Gonnermann, 2008; Parfitt & Wilson, 1994). Subplinian and plinian eruptions are more typical for silicic magmas, where the explosive nature of the eruption is thought to be associated with brittle magma fragmentation. The latter is unlikely to occur in basaltic magmas because of their low viscosity (e.g. Giordano & Dingwell, 2003; Houghton & Gonnermann, 2008), yet several volcanoes are known to have hosted plinian eruptions of basaltic magma (Sunset craters – Allison et al., 2021; Masaya – Bamber et al., 2020; Etna – Coltelli et al., 1998; Tarawera – Houghton et al., 2004; Kīlauea – McPhie et al., 1990).

In this context, the 3930 BP subplinian Fall Stratified (FS) eruption of picritic magma at Etna represents an extreme example of this mystery. The magma's high temperatures and H_2O concentration, and low SiO_2 concentrations and crystallinity, all act to lower viscosity (Coltelli et al., 2005; Kamenetsky et al., 2007), and yet this eruption was one of Etna's most explosive. The mystery of how to explosively erupt a low viscosity picritic magma is highlighted by their rarity; Coltelli et al. (2005) point out that the FS eruption is the only known subplinian eruption of picritic magma.

The uniformly primitive population of olivines within the FS magma (Fo 90–91) requires relatively fast magma ascent from at or near the Moho to avoid reequilibration toward lower forsterite compositions (e.g. Ruprecht & Plank, 2013). Furthermore, the high density of picritic basalt makes it difficult to ascend through the entire span of the crust (Anderson, 1995), and requires that the vapor phase remains coupled with the melt in order to avoid stalling in the mid crust (Corsaro and Pompilio, 2004).

It has been proposed on the basis of experiments, modeling, and field observations of geysers, that the plume height (and explosivity) of an eruption is positively correlated with its source depth (Namiki & Manga, 2006; Reed et al., 2021). Shock tube experiments on bubble-bearing viscoelastic fluids show that more violent fragmentation occurs for larger pressure drops and initial bubble volume fractions (Namiki & Manga, 2006). Greater source depths and higher vesicularity mean more potential energy to be converted into kinetic energy and consequently faster decompression.

Coltelli et al. (2005) propose that the FS eruption was propelled by high volatile concentrations (in particular CO_2) causing early exsolution deep in the crust and consequently high rates of magma decompression. We aim to test this hypothesis by determining the primary volatile concentrations and decompression rates of the magma. Ultimately, we want to understand how a picritic magma is able to ascend through the entire crust without stalling, mixing with other magmas, or crucially, losing its vapor, in order to erupt with the most explosive intensity ever documented for a picritic magma.

1.1 Background

The Fall Stratified eruption of Etna (3930 BP) produced voluminous pyroclastic flow deposits (0.055 km^3 dense rock equivalent – Coltelli et al., 2005), which attained thicknesses of 110 cm at distances of 7 km from the vent. The plume height has been estimated as 18–20 km from isopleth mapping corresponding to estimated mass eruption rates of $3.4 - 5.2 \times 10^7$

kg/s and a high explosive energy (VEI 4, subplinian – Coltelli et al., 2005). As suggested by its name, the Fall Stratified eruption deposit consists of fine scale layering between finer and coarser lapilli. Coltelli et al. (2005) argue that the deposit reflects "the formation of a sustained eruptive column" and interpret the layering as reflecting oscillations in plume height and that the lack of lithics and fine particles supports a magmatic rather than phreatic origin of the eruption. The FS eruption marks an important event in Etna's history – the productivity of explosive eruptions doubled after the FS eruption (Coltelli et al., 2000) (Fig. 1b), suggesting that it may have fundamentally altered the magmatic plumbing system beneath Etna and/or signaled a change in the mantle melting process (Fig. 1a). This is supported by the FS magma's anomalously high Rb/Nb ratios, which is typically high in subducting slab fluids/melts and thus thought to signify high input from subducted material (Fig. 1a).

Previous work has established key compositional features of the FS magma (Correale et al., 2014; Corsaro & Métrich, 2016; Gennaro et al., 2019; Kamenetsky et al., 2007). The magma is notable for its picritic composition – unusual for Mt. Etna and not erupted since the FS eruption. Whole rocks have 12–17 wt% MgO, melt inclusions (MIs) have 9–10 wt.% MgO, and most olivines are Fo 89–91. Note that Coltelli et al. (2005) find Fo as low as 83 but values <88 are restricted to microlites, extreme rims, or cores in rarely occurring reverse zoned crystals. Other studies (Kamenetsky et al., 2007; Gennaro et al., 2019) find exclusively Fo 89–91 olivines. Most olivines are unzoned (Coltelli et al., 2005). Another unusual aspect of the FS whole rocks and MIs is the high CaO/Al_2O_3 ratios (1.1–1.5; Kamenetsky et al., 2007), higher than any other eruptions at Etna and any subduction-adjacent magma in the world (e.g. Turner & Langmuir, 2015). The tephra contains high Mg olivines, clinopyroxenes (Mg# 90–91), and Cr spinel. Inclusions of high Mg # clinopyroxenes within olivines indicate early crystallization – a sign of high pressures of crystallization (Kamenetsky et al., 2007)

and also consistent with the high CaO/Al_2O_3. Furthermore, high volatiles concentrations (~ 4 wt% H_2O, 3500 ppm CO_2) have been measured in MIs, giving equilibrium pressures of ~ 500 MPa (Gennaro et al., 2019; Kamenetsky et al., 2007).

A major issue with the FS samples is that MIs contain a vapor bubble that is typically coated in Ca-Mg carbonates (Kamenetsky et al., 2007). Therefore, despite the already high measured CO_2 concentrations in the MIs' glass phase, true CO_2 concentrations and inferred equilibrium pressures are likely to be even higher. Previous work over the past years has demonstrated that the CO_2 concentrations in MI bubbles may contain > 80% of the bulk melt CO_2 (e.g. Moore et al., 2015), and so it is of paramount importance to reconstitute the CO_2 in MIs before being able to estimate both the depth of MI entrapment and the primary volatile contents of the magma.

2. **Sample Description**

Tephra from the FS eruption was collected by Silvio Rotolo at the Torrente Fontanelle (see IGSN:10.58052/IEACB000Y for further details), and is the same sample as studied by Correale et al. (2014) and Gennaro et al. (2019). The tephra contains large (up to 5 mm) and euhedral olivine and clinopyroxene crystals, along with microcrystals of Cr-spinel (Coltelli et al., 2005; Gennaro et al., 2019; Kamenetsky et al., 2007). Olivine-hosted MIs show clear faceting with scalloped edges (Fig.2). When viewed down the **b** axis MIs are typically oval to spherical, while along **a** or **c** they show a hexagonal shape. The 'tips' of the hexagons correspond to a plane (010) with a halo of micro fluid inclusions (present around all MIs, Fig.2b). This texture has been described elsewhere and may indicate partial decrepitation (Anderson JR, 1974; Portnyagin et al., 2005). Cr-spinels are common inclusions in olivine, and occur in more than 70% of the studied MIs (Fig.2, supplementary data table). Clinopyroxene can also be seen as inclusions within olivine (Fig. 2c) and were measured to have high Mg # (~90) by Kamenetsky et al. (2007).

All MIs contain a vapor bubble accounting for 3–10 vol% of the MI volume (Supplementary data table). There are no anomalously large bubbles, and bubble volume fraction correlates with MI size, typical of shrinkage bubbles and not those that are co-entrapped (Steele-MacInnis et al., 2017). The bubbles are typically coated in Ca-Mg-bearing carbonates (Fig. 2b and Kamenetsky et al., 2007). Many olivines contain clearly decrepitated MIs, characterized by an abnormally large vapor bubble and patterns of fluid inclusions radiating from the MI along planar cracks (Fig. 2a) – these were avoided for further study. For modeling H^+ and Fo profiles within the olivine, we selected inclusion-free, euhedral olivines. Crystal orientation was determined from morphology and confirmed for 28 crystals with electron backscatter diffraction.

3. **Methods**

We used a suite of analytical and experimental methods. Novel techniques are highlighted here, while routine methods are detailed in the supplement.

Rehomogenization experiments

In order to redissolve the shrinkage bubble and associated carbonate back into the melt, we attempted to rehomogenize the MIs using a piston-cylinder, as in Rasmussen et al. (2020). These attempts were unsuccessful, likely because the quench rate was not fast enough (supplement). We had better success using a vertically oriented internally heated pressure vessel (IHPV) at the Institute of Mineralogy, Leibniz University in Hannover, which has faster quench rates and proved an effective tool for high-pressure rehomogenization experiments with MIs (e.g. Mironov et al., 2015). Pt capsules were filled with MI-bearing olivines with and without de-ionised water and held at ~ 4 kbar and temperatures of 1250, 1280, and 1330 ^{o}C for ten minutes (supplement).

FTIR – glasses

H_2O and CO_2 MI concentrations (n=36) were measured on the Thermo Nicolet iN10 at Lamont-Doherty Earth Observatory. We paid particular attention to the baseline under the carbonate peaks (Shi et al., in revision). Full details are in the supplement.

FTIR – olivine

H_2O concentration profiles (n=18) were measured in doubly polished olivine wafers on the Thermo Nicolet iN10 at Lamont-Doherty Earth Observatory (Fig. 3). Barth et al. (2023) found good agreement between different peak-specific diffusivities so we consider bulk H_2O by summing the total area under the baseline-subtracted spectra. Full details are in the supplement.

SIMS

Rehomogenized MIs were fragile and developed cracks when intersected by polishing. Therefore, FTIR was not an option for the rehomogenized MIs, which were singly polished and analyzed by SIMS. Volatile abundances in rehomogenized MIs (n=26) were measured using a Cameca IMS 1280 multi-collection ion microprobe at CRPG-CNRS-Nancy. The calibration for C during this session was noisy and deviated significantly from typical calibration curves for the same instrument (Supplementary data table). To check the calibration, one rehomogenized MI and two check standard glasses were removed from the indium mount, doubly polished, and measured by FTIR. These values were then used as the calibration line (Supplementary data table). A second SIMS session was conducted at Caltech in 2022, primarily to verify the H_2O data, and a reasonably good agreement was found (Supplementary data table).

EPMA

Major elements for MIs and adjacent spots in their host olivines (n=49) were collected by electron microprobe analysis (EMPA) at the Smithsonian Institution using a JEOL JXA-8530F Hyperprobe. Major, minor and trace element profiles in olivine (n=8) were measured

using EPMA by a Cameca SX-5 with 5 WDS spectrometers at the American Museum of Natural History (AMNH).

Diffusion Modeling – H_2O

In order to determine magma ascent rates, we performed diffusion modeling of H_2O concentration profiles in olivines, which is sensitive to ascent rate in the depth region in which H_2O is degassing from the magma (~0–15 km depth). Our methods mostly follow those in Newcombe et al. (2020), except that we do not fix the final (shallowest) pressure. Instead, we solve for both the best-fit decompression rate and final pressure. Full details are in the supplement.

Diffusion Modeling – Forsterite

To estimate timescales of ascent from storage to eruption, we performed diffusion modeling of forsterite in eight unhomogenized olivine crystals. All profiles show a decrease from a central plateau towards the rim over a lengthscale of 50 – 100 μm for all analyzed elements (Ni, Mn, Ca, Al, forsterite), regardless of their diffusivity (Fig. 4). Al is considered to be almost immobile in olivine at magmatic temperatures over timescales of decades (Spandler & O'Neill, 2010), while Ni, Mn, Ca and Fe-Mg all diffuse faster. Thus, the lack of decoupling between elements indicates that the zoning we observe was dominantly generated by crystal growth, and that there was insufficient time to modify these profiles by diffusion. Furthermore, due to diffusive anisotropy in olivine, where Fe-Mg interdiffusion is 6 times faster along the **c** than the **a** axis (Dohmen & Chakraborty, 2007), we would expect to see different diffusive lengthscales along different crystallographic directions. The similar zoning lengthscales of forsterite content along **a** and **c** also argues for growth-dominated zoning.

We used a combination of forward and inverse modeling to obtain the maximum timescale in which Fe-Mg growth-zoning can be preserved for each measured profile along the **c** axis (supplement). This would give the maximum residence time at magmatic

temperatures between crystal entrainment near the Moho and quenching upon eruption. To calculate this diffusive decoupling timescales for Fe-Mg interdiffusion, we used the measured growth profile as the initial condition. This assumes that the whole rim grew instantaneously, where the start of the growth rim is marked by the decrease of Al from core values. We then modeled Fe-Mg diffusion until the model curve can be considered sufficiently decoupled from the initial growth conditions, accounting for analytical uncertainty. Modeling was performed using DFENS (Mutch et al., 2019, 2021) – full details in the supplement.

4. Results

4.1. IHPV rehomogenization experiments

After ten minutes of heating at 1250, 1280, and 1330 °C in the IHPV, the MIs exhibit a range of textures. All MIs become darker-colored after heating (Fig. 5), which may reflect the presence of Fe-bearing nanolites or an increased $Fe^{3+}/\Sigma Fe$ (Lerner et al., 2021). Some MIs are glassy and still contain a single vapor bubble, although comparing photos taken before and after the experiment shows that the bubbles have shrunk and moved during the experiment (Fig. 5a,b). Some MIs become very dark and speckled (with μm-scale bubbles or crystals) throughout (Fig. 5i,j), while others are glassy inside but have speckled surfaces (Fig. 5c-h).

For further analysis, MIs which had resorbed their bubble were prioritized – no MIs at 1250 °C, and only two MIs at 1280 °C (Ol8, Ol29) were chosen. All available MIs from the 1330 °C runs were analyzed.

4.2. Major and minor elements

The measured chemical compositions of the MIs and their host olivines agree well with those of Kamenetsky et al. (2007), Corsaro and Métrich (2016), and Gennaro et al. (2019) (Fig. 6). We correct for PEC using MIMiC (Rasmussen et al., 2020) calculating the partition

coefficient, K_d, from Toplis (2005) fixing Fe^{3+}/Fe_T to 0.32 based on microXANES measurements in Gennaro et al. (2020).

These calculations suggest minor PEC – up to 8%, with an average of 3%. Several MIs appear to have excess olivine – a possible sign of reheating. MIs show a limited range in all major and minor elements, and host olivine forsterite contents are equally restricted (90.3 – 91.2 %) – there is no evidence for significant fractionation (Fig. 6). Entrapment temperatures calculated from MIMiC are 1196 $\pm$11^{o}C (supplementary data table).

One remarkable characteristic of the Etna FS MIs is their extremely low Al_2O_3 (9.1 – 11. wt%) and high CaO (13.5 – 15.5 wt%) concentrations. While low Al_2O_3 can be achieved by high pressures of melting, the combination of high CaO and low Al_2O_3 points to a high CO_2 concentration in the source (Dasgupta et al., 2007; Lara & Dasgupta, 2022) or the involvement of clinopyroxene reaction processes (Danyushevsky et al., 2004).

The homogenized MIs show evidence for significant melting of the olivine host, as well as Fe-Mg exchange (MgO concentrations up to 18.5 wt%), which is common in these types of experiments that overheat the MIs (e.g. Rasmussen et al., 2020). When they are corrected for these processes, they overlap with the compositions of the unhomogenized MIs (Fig. S7).

4.3. Volatiles

Unhomogenized MIs show a weak positive correlation between H_2O and CO_2 with ranges of 2.5–4.9 wt% and 1910–3190 ppm, respectively (Fig. 7c). After PEC correction, these values are slightly lower due to the effect of dilution and are in the range 2.3–4.9 wt% and 1890–3110 ppm. In agreement with Gennaro et al., 2019, we do not find a correlation between H_2O concentrations and MI size (Fig. 6d, see supplement for details on size calculation), suggesting that the MIs have not undergone significant water loss during ascent (e.g. Qin et al., 1992). FTIR values for H_2O and CO_2 overlap with those in Gennaro et al. (2019),

although their SIMS measurements are offset to higher concentrations for both volatiles (supplement).

Homogenized MIs show a range of CO_2 concentrations from 4900 to 9600 ppm – a clear increase from the unhomogenized MIs (Fig. 7c) that is on average two-fold. Four of the measured MIs have a single remaining vapor bubble, and these MIs fall to the low end of the range of CO_2 concentrations (open black circles, Fig. 7c). Nine homogenized MIs contain multiple small bubbles at their edge; however, this does not appear to affect their CO_2 concentrations (purple vs. red circles, Fig. 7c), as found in Rasmussen et al. (2020). All of the homogenized MIs have μm-scale phases (crystals and/or bubbles), primarily lining the MI wall, but in some cases distributed in the interior of the MI. At present, we do not know what these phases are, and it is possible that they contain some CO_2, which would make our measurements lower bounds on the total amount of CO_2 in the MIs. Furthermore, the 'haloes' of secondary fluid inclusions surrounding all inclusions even before homogenization (Fig. 2) may indicate partial decrepitation, in which case the amount of CO_2 in the MIs at the time of entrapment may have been higher still.

Homogenized MIs have a narrower range and higher H_2O concentrations than unheated (Fig. 7c). This is unlikely to be the result of H_2O diffusing through the olivine from the experimental capsule since the experiments only last ten minutes, and we observe no systematic difference between dry and wet experiments. We cannot rule out that this is an analytical discrepancy – three unhomogenized and one homogenized MIs were measured by both SIMS and FTIR and the methods show discrepancies up to 0.85 wt.%, with the FTIR values exhibiting a wider range than the SIMS (supplement). It is possible that the FTIR measurements on unheated MIs underestimate H_2O concentration due to saturation of the detector. However, this would not explain the observed (albeit weak) H_2O-CO_2 correlation (Fig. 4c). Furthermore, we would expect the thickest wafers to give the lowest H_2O values,

which is not observed (Fig. S3). Alternatively, there may be hydrous phases on the walls of the MIs (although we note that none were found by Raman spectroscopy – Kamenetsky et al., 2007) or H_2O in the vapor bubble prior to homogenization, which is added back into the melt during homogenization (Esposito et al., 2016; Portnyagin et al., 2007).

The homogenization experiments do not appear to have altered the MI S or Cl concentrations (Fig. 7e), suggesting that they are not stored in the vapor bubble in significant quantities. In agreement with the results of Gennaro et al. (2019) and Corsaro and Métrich, (2016), we find that S does not correlate with CO_2 or H_2O, although it strongly correlates with Cl for both the homogenized and unhomogenized MIs (Figs. 7e,f,g). The S-Cl correlation is surprising since Cl and S are not expected to degas at such high pressures (> 500 MPa) (e.g. Ding et al., 2023). Neither correlate with Ni or Fo of the host olivine, or any indices of fractionation (e.g. K_2O). Cl and S variations may thus be indicative of primary melt heterogeneity (as is present in other trace elements – Kamenetsky et al., 2007).

4.4. ***Diffusion modeling***

4.4.1. ***H_2O***

All olivines appear zoned in H_2O concentration along **a** with no central plateaus, indicating that diffusion has reached the center of each olivine. Central H_2O concentration ranges from 14 to 33 ppm. Edge concentrations range from 6 to 25 ppm. An example Monte Carlo model run can be seen in Fig. 8. There is a positive correlation between the diffusivity and decompression rate while other parameters exhibit weak or no correlation with decompression rate. Therefore, within the parameter ranges studied here, the uncertainty in diffusivity accounts for the largest source of uncertainty in decompression rate. We emphasize, however, that the diffusivity used was determined specifically for Etna FS olivines in a companion study (Barth et al., 2023). The best-fit decompression rate for all 18 olivines is remarkably uniform (Fig. 8b). A histogram of all best-fit decompression rates

shows a lognormal distribution centered at 0.47 MPa/s with 95 % confidence bounds of 0.16 and 1.28 MPa/s. Assuming an average crustal density from the surface to 15 km depth of 2600 kg/m^3 from Corsaro & Pompilio (2004), this corresponds to 17.5 m/s with 95% confidence bounds of 6 and 49 m/s.

4.4.2. ***Forsterite***

The median diffusive decoupling timescales determined from the Bayesian inversion (Mutch et al., 2021) range from one to five days for the different olivines. Uncertainties on these timescales propagated from those in temperature, fO_2, pressure, and diffusion coefficients vary for the different olivines and are -2 days and +4 days on average (full results in supplementary data table). Note that we can only constrain an upper bound on timescales since there are no diffusion profiles to model.

These results indicate that the olivines must have ascended from storage at near Moho depths to the surface at rates of 0.05 – 0.35 m/s or faster. If ascent were slower, the olivines would show signs of reequilibration with the surrounding olivine-free granulitic crust (Corsaro & Pompilio, 2004; Tonarini et al., 1996). Recent experimental results from Shea et al. (2023) show that the presence of a surrounding melt may enhance cation diffusion in olivines by up to a factor of 10. While the mechanism for this effect is still not well understood, it is thus possible that the true ascent velocities are even faster than the above estimates.

5. Discussion

5.1 Reconstructed CO_2 concentrations

5.1.1 Comparison of MIMiC and homogenization experiments

Since the discovery of the importance of MI vapor bubbles, several methods have been developed to account for the CO_2 stored within them. These techniques fall broadly into three categories: (1) dissolving the vapor bubble back into the MI with rehomogenization

experiments before measurement, (2) using an equation of state and measuring or modeling the size of the bubble, and (3) measuring the CO_2 in the vapor bubble with Raman spectroscopy. These methods are described and compared more fully elsewhere (Moore et al., 2015; Rasmussen et al., 2020; Wallace et al., 2021). We compare the results of our rehomogenization experiments with the modeling approach of Rasmussen et al. (2020) using the publically available MIMiC code. MIMiC calculates bubble volume at the closure temperature for CO_2 (the temperature at which CO_2 diffusion effectively ceases), using an equation of state approach, and taking into account deformation of the host olivine. The model input includes the measured chemistry and sizes of the MIs and olivine hosts and an estimate of cooling rate (we assume a cooling rate of 10 ºC/s, as recommended for lapilli-sized clasts – Rasmussen et al., 2020).

There is close agreement between the CO_2 concentrations predicted by MIMiC using the unheated MIs and those measured by SIMS in the homogenized MIs, giving a spread of 4400–8200 and 4900–9600 ppm, respectively (Fig. 7c). This suggests that minimal CO_2 is stored in the tiny phases lining the walls of some of the rehomogenized MIs (Fig. 7a,b).

5.1.2 Pressure of magma storage

One of the primary ways to estimate magma storage depth is by calculating saturation pressures based on the H_2O and CO_2 concentrations within MIs. Therefore, restoring the CO_2 concentrations in the vapor bubbles has implications for the depths of magma storage. Note that these pressures are minima because they assume that the magma is saturated with a H_2O-CO_2 vapor phase. There are a range of solubility models for mixed volatiles, which have been calibrated over different pressure, temperature, and compositional space. MagmaSat (Ghiorso & Gualda, 2015) has the best coverage near the Etna FS composition and temperatures (Fig. S4,5). Duan (2014) also has good coverage, although is not implemented in the python package VESIcal (Iacovino et al., 2021). The models from Iacono-Marziano et al. (2012),

Allison et al. (2019), and Allison et al. (2022) are calibrated on Etna magma but because the FS magma is so unusual for Etna it lies outside their compositional range (Fig. S4,5). The model of Dixon (1997) has good compositional coverage but does not extend to pressures higher than 500 MPa, and Iacono-Marziano et al., 2012 suggested that the Dixon (1997) calibration range was only reliable up to 100 MPa.

MagmaSat and Duan (2014) give the highest saturation pressures (676–819 and 645–1032 MPa, respectively, corresponding to the range in CO_2 concentrations in homogenized MIs without single vapor bubbles), while the solubility models in Iacono-Marziano et al. (2012), Allison et al. (2019), and Allison et al. (2022) give lower pressures (405–524, 415–649, and 343–547 MPa, respectively). Based on the different lithologies with depth beneath Etna (Corsaro & Pompilio, 2004), we iteratively solve for the magma storage depth and average density of the overburden. This gives an average overburden density of 2720 kg/m^3 and depth of 30 km for the highest initial pressure of 819 MPa, and average density and depth of 2650 kg/m^3 and 24 km for the shallowest initial pressure of 676 MPa. These depths closely align with entrapment depths determined from olivine-hosted CO_2-rich fluid inclusions of 21–24 km of samples from Aci Castello and Mt. Maletto (Kamenetsky & Clocchiatti, 1996). We now examine how these depths relate to the crustal structure beneath Etna.

Although the regional Moho beneath eastern Sicily is on the order of 30 km (e.g. Accaino et al., 2011), detailed seismic imaging offshore of Etna finds a mantle upwarp (Nicolich et al., 2000) associated with a major tectonic feature, the Alfeo Fault System (Dellong et al., 2018). Nicolich et al. (2000) map a thinning of the Moho from 25 to 17 km immediately offshore of Etna, and suggest that the location of Etna is related to this tectonic feature. We thus consider the Moho beneath Etna to be in the range of 17–25 km and that the FS magma ascended from storage at or beneath the Moho. Viewed another way, our volatile saturation pressures can help to constrain the Moho depth, since the high and uniform

forsterite content (90–91) of the FS olivines requires that the olivines must be coming from storage at or below the Moho, since they cannot have equilibrated with the olivine-free mafic granulites of the lower crust (Corsaro & Pompilio, 2004; Tonarini et al., 1996). As noted by Corsaro & Pompilio (2004) the FS magma "represents a primitive melt in equilibrium with the mantle". Crucially, the entrapment depths of the FS MIs means that the high CO_2 concentrations cannot have been the result of assimilation of the shallow carbonate crust, which is thought to extend to depths of ~ 10 km (Fig. 9, Corsaro and Pompilio, 2004).

5.2 Carbonate in the mantle source feeding the FS eruption

Here, we address the question of what generated the unusually high CaO/Al_2O_3 ratios (1.1–1.5) in Etna FS MIs and whole rocks (Fig. 10a, Kamenetsky et al., 2007; Corsaro and Métrich, 2016). The two primary hypotheses are involvement of 1) clinopyroxene-bearing lithologies or 2) carbonate in the magma's source.

High CaO MIs have been explained by melting/dissolution of clinopyroxene-bearing lithologies in general terms (Danyushevsky et al., 2004; Schiano et al., 2000) and specifically for the Etna FS magma (Correale et al., 2014; Corsaro & Métrich, 2016). However, the approach of Correale et al. (2014) relied on assumptions about melting and crystallization based on major element modeling which was not able to fit the FS compositions (see their Fig. 10). Corsaro and Métrich (2016) argue that the high Zr/Nb and low Ce/Y requires the melting of a clinopyroxene-bearing lithology, however measured ratios in FS whole rocks overlap with measured ratios for Hyblean peridotite xenoliths (Correale et al., 2014).

On the other hand, experiments have shown that addition of CO_2 to the mantle source can generate high CaO/Al_2O_3 ratios in the magma (up to 2.7), both by lowering Al_2O_3 and raising CaO in the melt (e.g. Dasgupta et al., 2007). In volatile-free peridotite, this level of CaO-enrichment and Al_2O_3 depletion can only be generated by melting at pressures above 4–5 GPa (Walter, 1998) – greater than typical arc melting pressures. Recent experiments with

H_2O- and CO_2-bearing fluids (Lara & Dasgupta, 2022) suggest that the Etna FS magma composition could be explained by the presence of a fluid with XCO_2 (molar $CO_2/(CO_2+H_2O)$) of ~ 0.1. Furthermore, the olivine compositions (namely their Ni, Mn, and Ca concentrations) are consistent with carbonate metasomatism of the magma's source, rather than involvement of pyroxenite (Fig. 10a; Ammannati et al., 2016).

Finally, there is a regional signature of carbonate metasomatism in the mantle. At Stromboli volcano, 115 km from Etna, isotopically heavy C ($\delta^{13}C$ -2.7‰ to -1.0‰), indicative of carbonate, was measured in bulk separates of high forsterite olivines from xenoliths of ultramafic cumulates thought to derive from the mantle (Gennaro et al., 2017). The authors propose that this reflects contamination of the mantle by C-rich sediments from the subducting slab. Magmas from the Hyblean district, ~60 km S of Etna show trace element and Sr-Nd-Pb isotopic signatures consistent with carbonatite metasomatism (e.g. Trua et al., 1998). C-rich fluid inclusions in wehrlitic xenoliths from Monte Vulture (~350 km N of Etna) further support carbonate metasomatism of the mantle (Carnevale et al., 2022). Below, we outline further support for the involvement of C-rich subducting sediments in the source of the Fall Stratified eruption.

Etna is situated away from the main Aeolian arc, and its location may be related to a tear in the subducting slab (e.g. Gvirtzman & Nur, 1999). A trace element subduction signature (enrichment in large-ion lithophile (LILE), depletion in high field strength elements (HFSE)) has been documented for Etna magmas since ~100 ka (Corsaro & Métrich, 2016; Schiano et al., 2001; Tonarini et al., 2001), including for the FS magma (Kamenetsky et al., 2007). Using the average H_2O value from our MIs (~ 4.7 wt%) and the Ce concentration in the whole rock (Correale et al., 2014) and MIs (Kamenetsky et al., 2007) gives a H_2O/Ce ratio of 750 and 500–1300, respectively – clearly above typical MORB values (100–300; Dixon et al., 2002), suggesting that a significant portion of the magma's H_2O was derived

from the subducting slab. Corsaro and Métrich (2016) show that the Cl/K_2O ratios of FS MIs are well above typical mantle values, suggesting that most of the Cl is derived from the slab (Fig. 10). High Cl/K_2O and CaO/Al_2O_3 ratios have also been found for other historical primitive eruptions at Etna: Mt. Spagnolo (15–4 ka) and Mt. Maletto (7 ka). Furthermore, Mt. Spagnolo and FS show a correlation between CaO/Al_2O_3 and degree of Cl enrichment. They are also the only two eruptions to show a positive correlation in S and Cl (supplement). Therefore, we propose that the high CaO/Al_2O_3 ratios and enrichment in Cl and S are reflecting a common process, likely input into the mantle of a fluid or melt that is rich in Cl, S, H_2O and CO_2 from a subducting slab, whether it was added just prior to the FS eruption or stored on long timescales in metasomatic phases in the mantle (Viccaro & Cristofolini, 2008).

5.3 Magma decompression rate

The combination of forsterite and H_2O diffusion modeling allows us to piece together the magma ascent rate all the way from source to surface (Fig. 9). The lack of diffusive zonation of forsterite within the olivine crystals is highly unusual and implies rapid ascent (> 0.1 m/s) from near Moho depths (24 – 30 km) to the surface in less than 1–5 days (Fig. 4). These rates are faster than those estimated for ascent from the Moho in the Borgarhraun eruption of Iceland (0.02–0.1 m/s; Mutch et al., 2019), which could be tied to the lower CO_2 concentrations (~600 ppm) and consequently shallower vapor saturation (~3 km) of the Borgarhraun magma.

The H_2O zonation profiles within the olivine crystals require average decompression rates of 0.47 MPa/s from depths of ~15 km to the surface. This is among the highest measured by diffusion chronometry for basaltic-intermediate eruptions (Barth et al., 2019; Cassidy et al., 2018), although faster rates have been found in the final few kilometers of ascent beneath Ambrym and Ambae/Aoba volcanoes (Moussallam et al., 2019, 2021) and for recent paroxysms at Etna (Giuffrida et al., 2018; Zuccarello et al., 2022). The most explosive

of these recent paroxysmal events attained plume heights of ~15 km, although it was significantly lower in volume (by a factor of ~25 – Coltelli et al., 2005; Corsaro et al., 2017) and was sourced from shallower depths (~1 km b.s.l.) than the FS eruption. Crucially, the ascent rates that we determine exceed those which have been experimentally shown to induce CO_2 supersaturation, which has been suggested as a mechanism for fragmentation of low-viscosity basaltic magmas (Pichavant et al., 2013).

In keeping with the uniformity of olivine and MI compositions, the decompression rates are also highly uniform. This supports the observation by Newcombe et al. (2020) that more explosive eruptions may have less variable decompression rate than lower energy eruptions, for which unsteadiness in flow rate may be more pronounced.

To assess whether the ascent rates that we derive are physically plausible, we apply the analytical expressions for the propagation of fluid-filled fractures driven by fluid buoyancy given by Davis et al., 2023. In their formulation, ascent rate is a function of fluid volume, density, viscosity and the elastic parameters of the host medium. Using a Monte Carlo approach, we calculate ascent rate and uncertainty by drawing parameters from normal distributions (Fig. S11) with the following mean and standard deviation: volume = 0.055 ± 0.005 km^3 (Coltelli et al., 2005), average density contrast between host crust and magma = 285 ± 100 kg/m^3 (supplement, fig. S10), and viscosity = 4.6 ± 0.5 Pas (calculated from the model by Giordano et al., 2008 on the average unheated MI composition). Note that this viscosity model includes the effect of H_2O but not CO_2, which could make the viscosity even lower (e.g. Di Genova et al., 2014). The Young's modulus of the crust is the least well-constrained parameter; we calculate a depth-average from the surface to 30 km of 89 GPa from Currenti et al., 2007 and use a large uncertainty of ± 30 GPa. If ascent starts at 24–30 km depth, the model predicts average ascent rates of 8–11 m/s (Fig S9). This suggests that

our calculated ascent rates from H_2O diffusion (mean of 17.5 m/s) and our lower bound from Fe-Mg interdiffusion (> 0.1 m/s) are reasonable.

5.4 Uniqueness of FS Eruption

Other primitive Etna magmas (Mt. Spagnolo and Mt. Maletto) show similar geochemical characteristics as the FS magma (Corsaro & Métrich, 2016), implying that these magmas may not be rare at Moho depths beneath Etna but that their signature gets destroyed with mixing and fractionation in the plumbing system. Unlike the FS magma, Mt. Spagnolo and Mt. Maletto magmas both show a significant range in geochemical indicators of fractionation (e.g. K_2O, MgO), indicating that they either mixed with more fractionated magma during ascent, or crystallized extensively themselves. Either scenario implies slower ascent for these two magmas compared to the FS magma, which may have allowed the escape of their volatile phases and hence lowered the eruption intensity.

The high CO_2 concentration of the FS magma and a consequently deep exsolved vapor phase may have initiated diking at Moho depths. Thus, the magma was still hot and had low viscosity when it began ascending, allowing it to propagate fast (8–11 m/s, as above). Either the transporting dyke fortuitously avoided shallow magma reservoirs, or else it was able to pass through relatively unhindered, perhaps because of its fast speed and/or the long hiatus of volcanic activity that preceded the FS eruption (Fig. 1b), which may have allowed shallow magma bodies to cool and solidify. The total pressure-drop and vesicularity during ascent is thought to affect the expansion velocity of the magma, and consequently the eruptive intensity (e.g. Namiki and Manga, 2006). Therefore, the FS magma's unhindered ascent from its deep storage pressures and its high volatile concentrations (particularly CO_2) may have been responsible for its high explosive energy.

6. Conclusions

The subplinian FS eruption of Etna was remarkable in terms of its primitive composition and high volatile concentrations. Previous studies underestimated the magma's CO_2 concentration by neglecting the MI vapor bubbles. In this study, we rehomogenized olivine-hosted MIs to resorb their vapor bubbles and carbonate back into the MIs. SIMS and FTIR measurements show that these rehomogenized MIs contain between 4900 and 9600 ppm CO_2, corresponding to magma storage pressures of at least 676–819 MPa (24–30 km). These depths are comparable to the seismologically estimated Moho (17–25 km) suggesting that MIs were entrapped in the mantle, and cannot have gained their CO_2 contents by dissolving the carbonate crust, which only extends to ~ 10 km depth. Instead, we argue that the MIs' high CO_2 concentration is derived from carbonate in the mantle source of Etna on the basis of MI CaO/Al_2O_3 ratios, olivine Ni contents, and isotopic measurements of C in high forsterite olivines from the nearby Stromboli volcano.

Diffusion modeling of H_2O and forsterite profiles in olivine crystals demonstrates the remarkably fast ascent of the FS magma. The forsterite profiles require that the magma ascended from near Moho depths to the surface in less than 1–5 days. Modeling H_2O profiles, which are sensitive to the region in which H_2O is degassing from the magma (<15 km depth), gives average decompression rates of 0.47 MPa/s or 17.5 m/s (assuming a lithostatic pressure gradient).

We propose that this eruption may record a link between the primary magma composition and eruption style; the unusually explosive nature of this picritic eruption was driven by the high CO_2 concentrations, imparted to the magma by subducted carbonate in the mantle source. This CO_2 caused deep exsolution of a vapor phase which may have initiated fast diking all the way from the Moho to the surface, relatively uninterrupted by fractionation and mixing in the crust. The magma's deep origin, high volatile contents, and consequently rapid ascent, all acted to increase the explosive intensity of this eruption.

Acknowledgements

The authors would like to thank Dave Walker for his help with the piston-cylinder experiments – his insight, intuition, and constant optimism were invaluable. We would also like to thank Philipp Beckmann for his help in performing the IHPV experiments, Yunbin Guan for making SIMS measurements at Caltech, and Céline Martin for microprobe measurements at AMNH. NM and FH acknowledge support from the joint DFG-RFBR project (HO1337/44-1, DFG to FH and 20-55-12013, RFBR to NM). This work was funded by NSF grant number EAR-1524542 to TP.

Figures

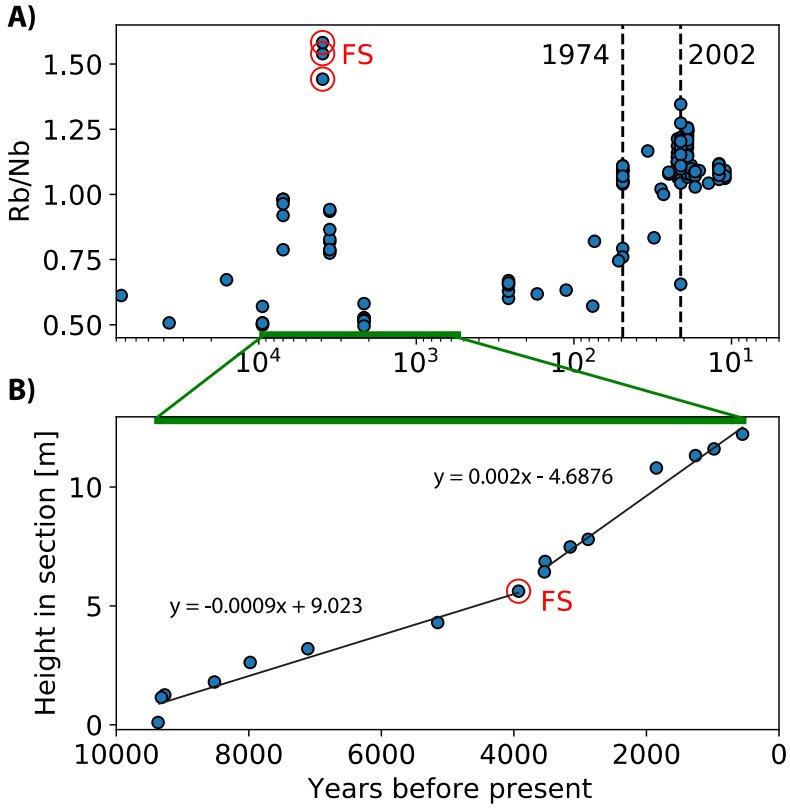

Figure 1a) Rb/Nb ratios over time highlighting uniqueness of FS eruption. Note the log scale of time, in order to show data from recent eruptions clearly. b) Height and age of Etna eruption deposits in stratigraphic section showing doubling of bulk sedimentation rate after the Fall Stratified Eruption. Also note hiatus of large eruptions for the ~1000 years prior to FS. Data and references listed in supplementary data table.

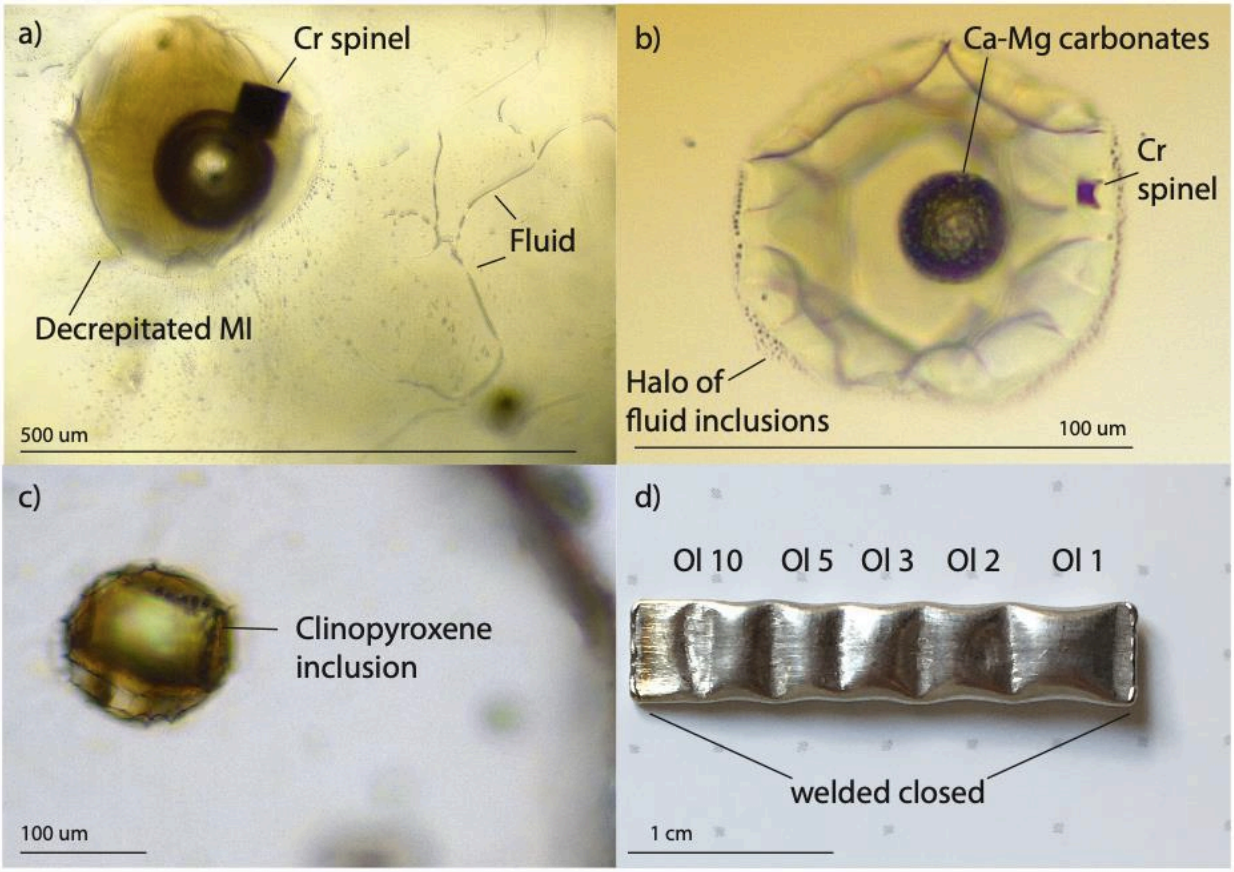

*Figure 2. (a) Decrepitated MI containing a Cr-spinel with fluid inclusions radiating away from the MI along a planar crack. Note the large bubble size, which is a feature of these decrepitated MIs. (b) Typical Etna FS MI containing tiny Cr-spinel and vapor bubble lined with Ca-Mg carbonates. Photo is looking down **b**. The halo of tiny fluid inclusions around the MI is ubiquitous in this sample. (c) Inclusion of melt and clinopyroxene within olivine. (d) capsule for IHPV experiments. Individual olivines are separated by gently crimping around them in order to compare before and after photos.*

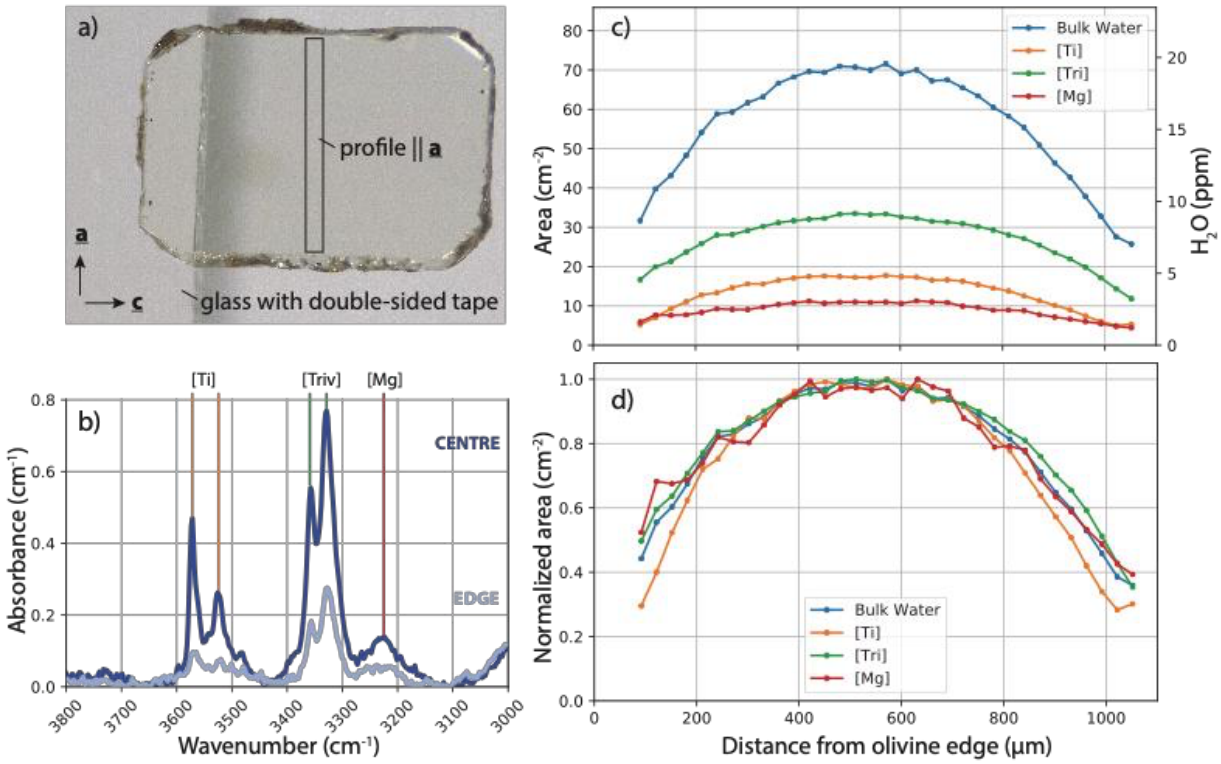

*Figure 3. H_2O concentration profile in olivine along the crystallographic **a** direction measured with FTIR. (a) Photograph of olivine wafer taken down **b** [010]. (b) FTIR spectra with baseline subtracted taken in the centre (dark blue) and edge (light blue) of the olivine. Absorption peaks represent OH^- bonds associated with different point defects. Bulk H^+ concentration estimated by summing area under spectra from 3600 – 3100 cm^{-1}. (c) Defect-specific profiles along crystallographic **a** direction. Area is converted to H_2O concentration using the Withers et al. (2012) calibration and multiplying by a correction factor to account for the light which would be absorbed in the direction of the raypath. (d) Normalised defect-specific profiles.*

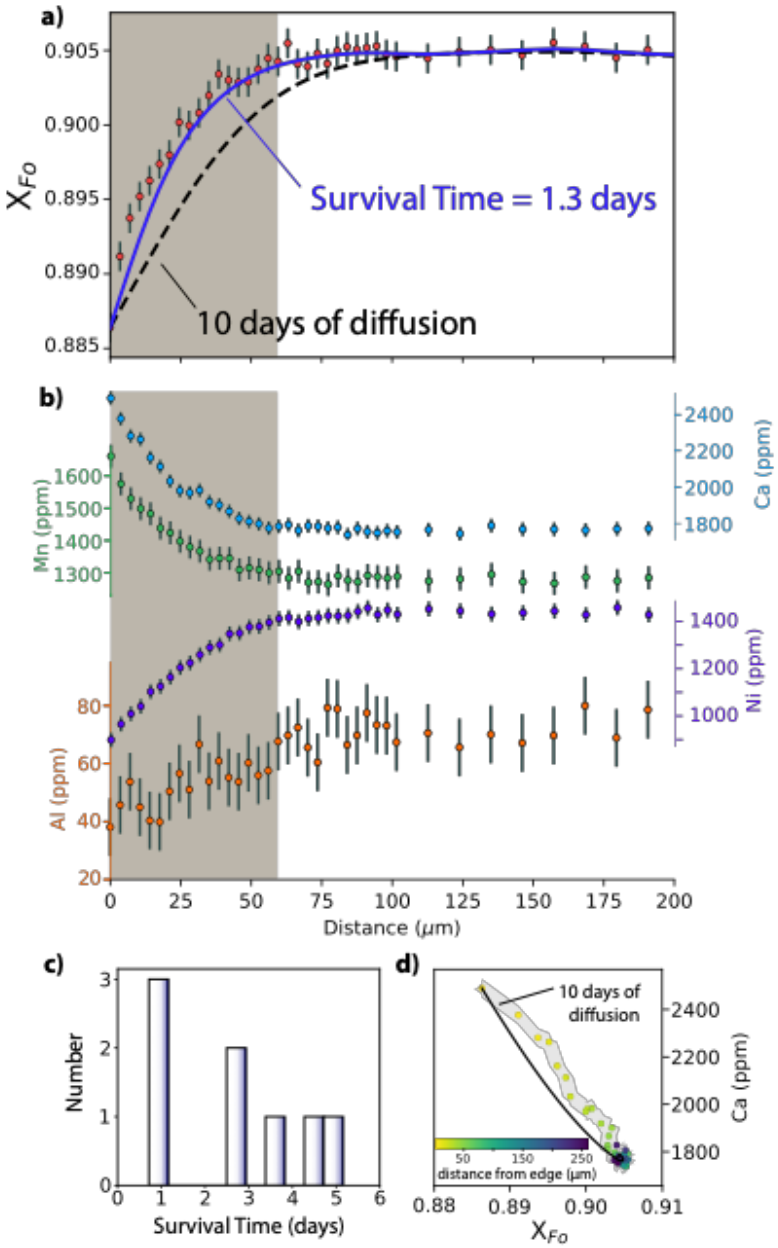

Figure 4. a, b) Major and trace element diffusion profiles in one olivine (Ol52) along [001], the fast direction for Fe-Mg diffusion. Note the similar lengthscales of zonation profiles for all elements (shaded region), regardless of their diffusivity. c) histogram of survival times based on forsterite zonation profiles (see text for description of calculation). d) Initial condition for Fo diffusion modeling calculated from linear relationship between Fo and Ca. Black reference curve in a) and c) shows effect of 10 days of diffusion.

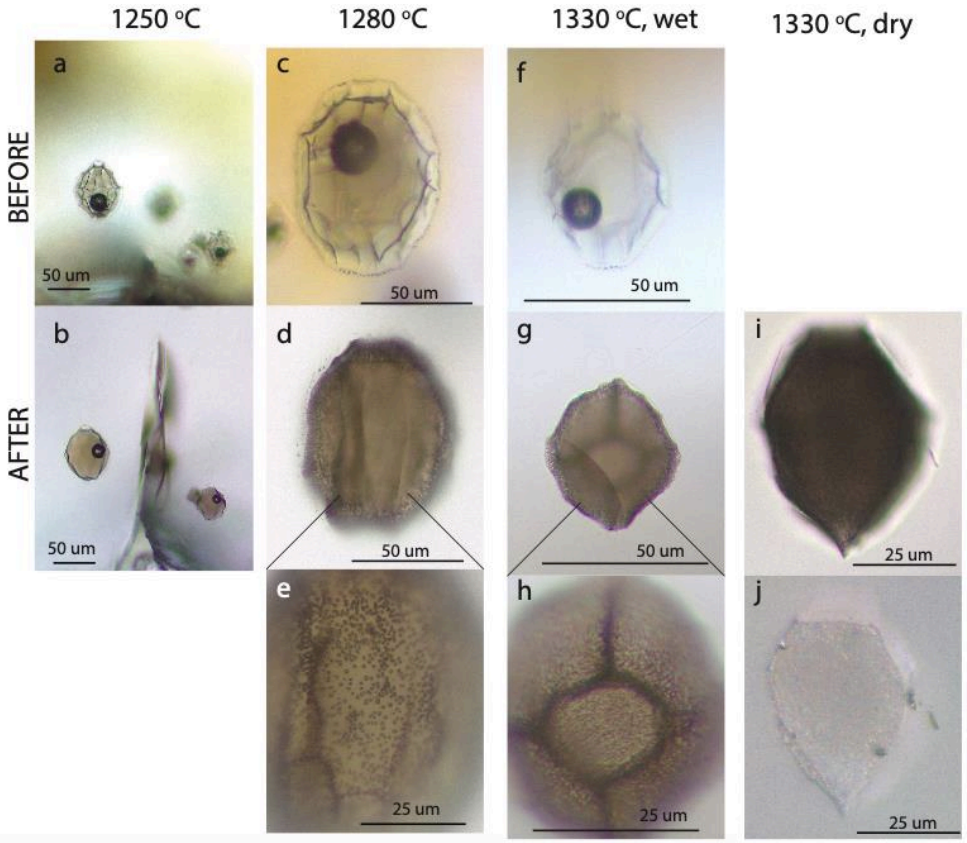

Figure 5. Before and after photographs of MIs at different experimental temperatures and conditions. There was no 'before' photo for the MI heated in dry capsule at 1330 °C. (a) and (b) show photos of MIs before and after heating at 1250 °C under wet conditions. Note the MI color becomes darker, the faceting less distinct, the carbonate lining the bubble dissolves, and the bubble shrinks and moves. (c) and (d) show photos for MI before and after heating at 1280 °C under wet conditions. Bubble is fully dissolved and MI interior is glassy. (e) Photograph focused on bottom surface of MI and zoomed in to show tiny bubbles and/or crystals lining MI wall. (f-h) are same as (c-e) but for 1330 °C. (i) and (j) show transmitted and reflected photographs of MI heated at 1330 °C under dry conditions. MI becomes dark and speckles can be seen in reflected light throughout interior of MI.

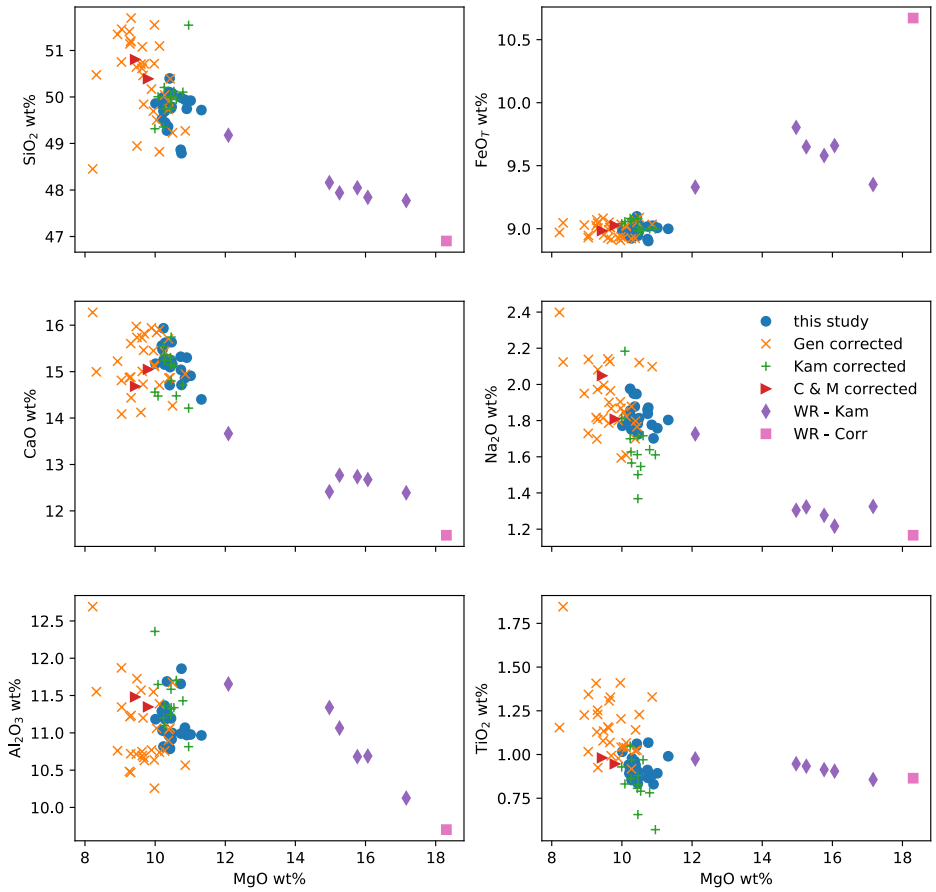

Figure 6. PEC-corrected major element composition of unheated MIs from this study (blue circles). Data from literature for Etna FS shown for comparison (Gennaro et al. (2019), orange crosses; Kamenetsky et al. (2007), green plus; Corsaro and Métrich (2016), red triangle). Whole rock (WR) from Kamenetsky et al., 2007 (purple diamond) and Correale et al., 2014 (red square) and shows variable degrees of crystal accumulation. All data is normalized to 100% volatile-free. Note that data for other MI studies was corrected for PEC using MIMiC with the same parameters as the data in this study (see supplementary data table).

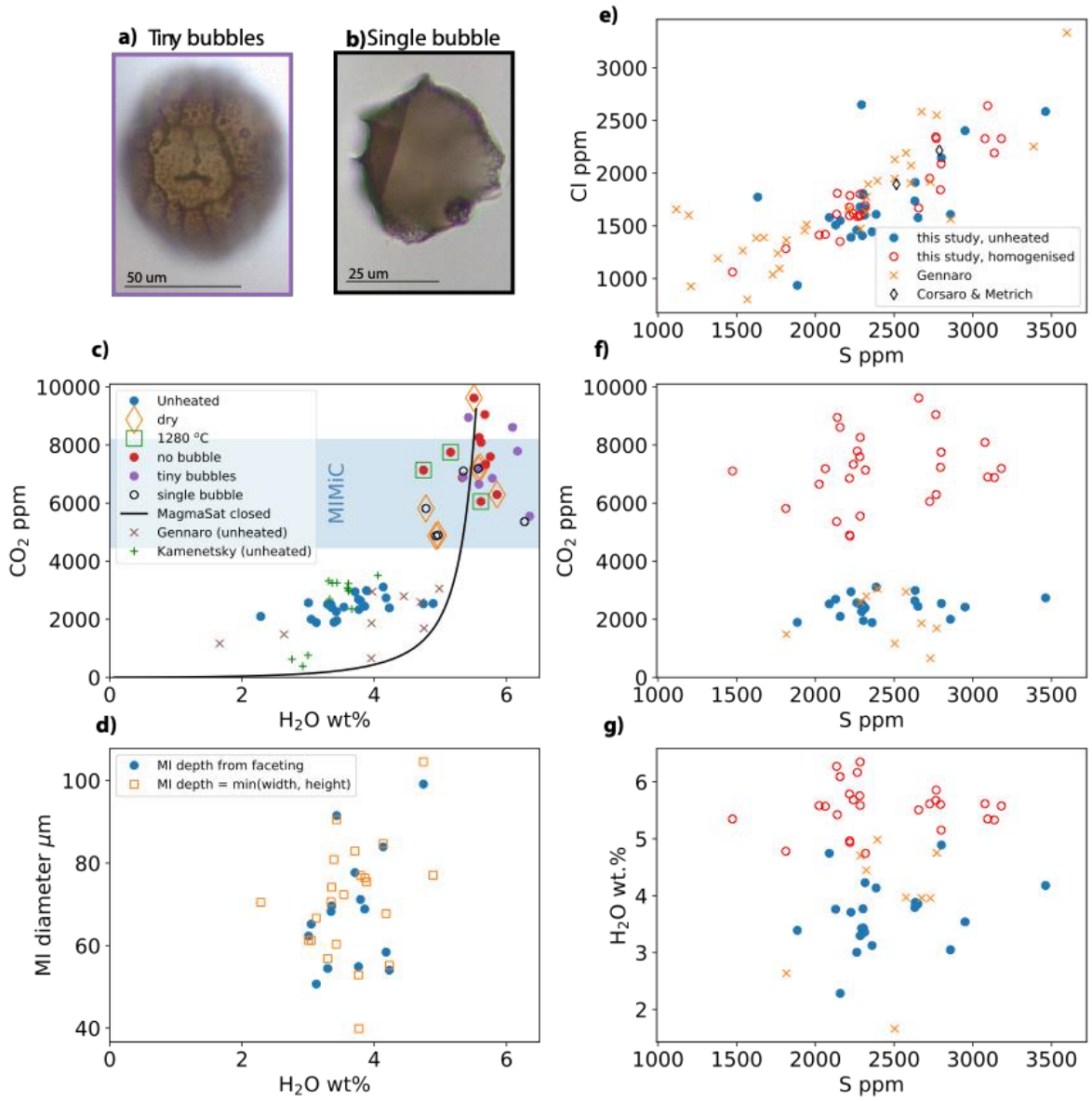

*Figure 7. Volatiles in homogenized and unheated MIs. (a, b) Examples of MIs with a single vapor bubble and multiple tiny bubbles. (c) H_2O versus CO_2 for homogenized and unheated MIs. Dry experiments shown with orange diamonds. Experiments at 1280 °C shown with green squares (all others are at 1330 °C). MIs with a single vapor bubble (open circles) plot to lower CO_2 concentrations. However, MIs with multiple tiny bubbles (purple circles) do not have less CO_2 than those without (red circles). Note that unheated MIs show scattered positive trend. CO_2 predicted by MIMiC modeling of unheated MIs (shaded blue) is similar to measurements of homogenized MIs. MagmaSat closed system degassing trend used in diffusion modeling of H^+ in olivine profiles is overlain. (d) H_2O versus MI diameter measured from photographs in two ways for unheated MIs. The first method is detailed in the supplement and uses MI faceting to predict MI depth from photographs taken down the **b** axis (blue circles). This method is only possible for MIs which were photographed down the **b** axis. The second method assumes that MI depth is equal to the shortest MI dimension measured in the photograph (orange squares). (e) Cl versus S measured by EPMA. Note the strong, approximately linear, correlation between S and Cl in all three studies (Gennaro et al., 2019; Corsaro and Metrich, 2016; this study), and for both unheated and homogenized MIs. (f) CO_2 versus S, symbols same as in (e). CO_2 measured by FTIR for unheated MIs and SIMS for homogenized MIs. (g) H_2O versus S, symbols same as in (e). Note that for data from Gennaro et al., 2019, only H_2O and CO_2 determined by FTIR are shown.*

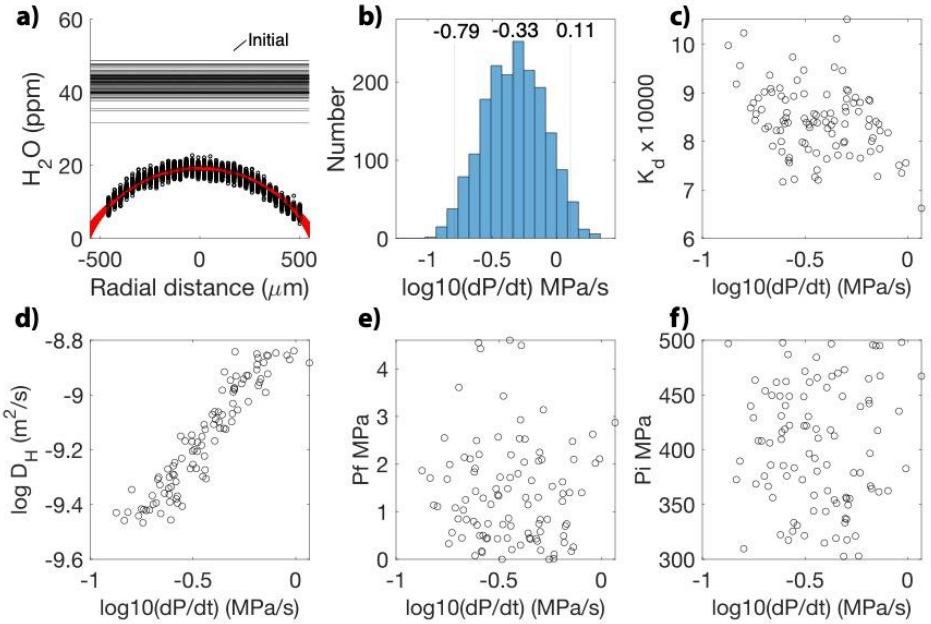

*Figure 8. Example Monte Carlo run to constrain decompression rate and final pressure by modeling 1D H^+ diffusion along crystallographic **a** direction. (a) FTIR profile with noise added in black circles, model fits (red lines). Initial H_2O concentration chosen from normal distribution with mean of 42 ppm and standard deviation of 3 ppm (see text for details). (b) Histogram of best-fit decompression rates for all Monte Carlo runs for different olivines. Vertical lines show mean and 95 % confidence intervals (c) Partition coefficient, Kd, versus decompression rate. Kd is calculated as the ratio of initial H_2O concentration in olivine (shown in (a)) relative to magma, which is set by MagmaSat solubility model and initial pressure, Pi. (d) Diffusivity versus decompression rate shows a clear positive correlation – most of the uncertainty in decompression rate comes from uncertainty in diffusivity. Upper bound of diffusivity is set by fastest dehydrating rate measured (Ferriss et al., 2018), Lower bound is set by initial dehydration rate measured in* Barth et al. (2023)*. Final, Pf, (e) and initial, Pi, (f) pressure versus decompression rate show no relationship. Range of initial pressure chosen as the region in which H_2O begins significant degassing*

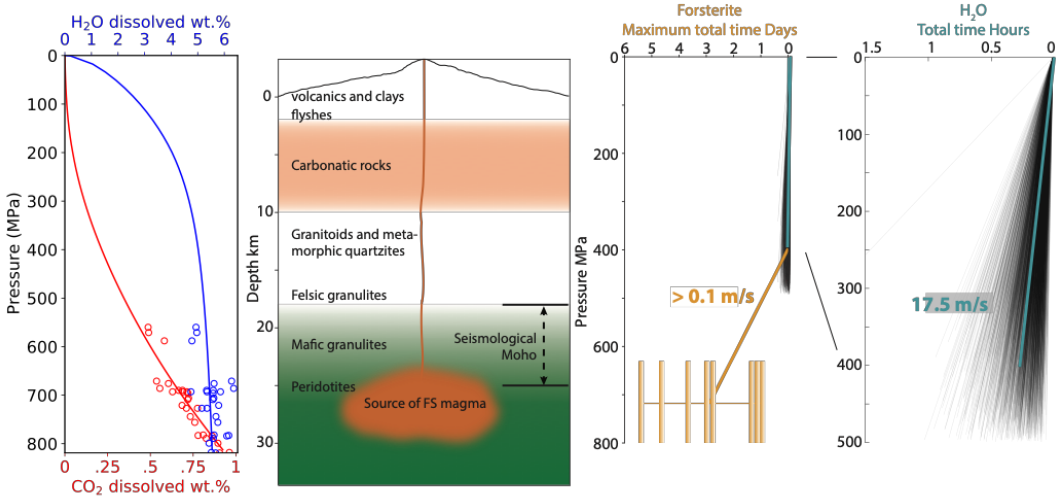

Figure 9. a) Degassing path modeled with MagmaSat for FS magma with MI saturation pressures determined with MagmaSat (Ghiorso & Gualda, 2015) *overlain in blue (H_2O) and red (CO_2) circles. Crustal section beneath Etna with lithologies from Corsaro and Pompilio 2004. Likely range of Moho depth from seismological observations shown by dashed arrow (see text for references). c) Maximum ascent times from storage to surface calculated from forsterite zonation modeling shown as vertical yellow bars. Vertical span of yellow bars represents uncertainty in storage pressure from range of MI volatile contents. Average ascent rate is 0.1 m/s and is shown by bold yellow line. Note that each bar represents a maximum, not best-fit, ascent time for one olivine. Ascent rate from H_2O Monte Carlo diffusion modeling shown by black lines, with mean ascent rate overlain in blue d) Zoom-in of H_2O diffusion model. Each black line represents results from a single Monte Carlo run. Average ascent rate is 17.5 m/s and is shown by bold blue line.*

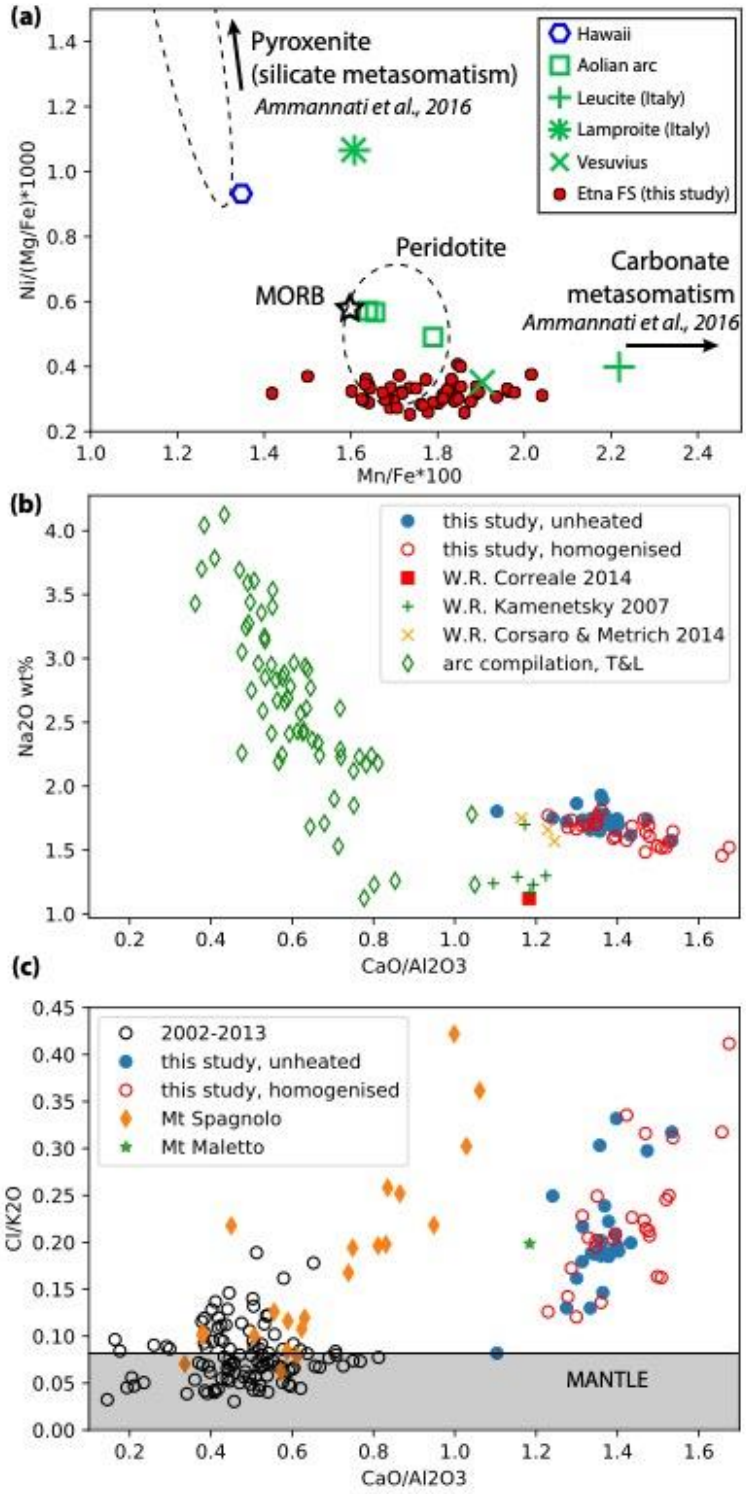

Figure 10. Evidence for carbonate in FS magma source (a,b) and involvement of subducting slab(c). (a) Olivine compositions from FS have low Ni concentrations, prohibiting a large role for pyroxenite in its source. Compositions for other Italian magmas (green) from Zamboni et al., 2017. Also shown are the compositions for peridotite and pyroxenite, as well as the expected trend for silicate and carbonate mantle metasomatism from Ammannati et al., 2016. (b) Whole rock and melt inclusions (this study) of the FS magma is outside of the global arc array (from samples with Mg# > 60, Turner and Langmuir, 2015) at low Na_2O and high CaO/Al_2O_3. (c) Comparison of Cl/K_2O for modern eruptions and three primitive eruptions at Etna (Mt. Spagnolo – Gennaro et al., 2019, Mt Maletto – Schiano et al., 2001, and Fall Stratified – this study). Modern eruptions have only moderately higher Cl/K_2O ratios compared with MORB, and individual eruptions do not show a correlation between CaO/Al_2O_3 versus Cl/K_2O. In contrast, all three primitive eruptions have high Cl/K_2O and CaO/Al_2O_3, and Mt. Spagnolo and FS show positive correlation between these ratios.

References

Accaino, F., Catalano, R., Di Marzo, L., Giustiniani, M., Tinivella, U., Nicolich, R., Sulli, A., Valenti, V., & Manetti, P. (2011). A crustal seismic profile across Sicily. *Tectonophysics*, *508*(1–4), 52–61.

Allison, C. M., Roggensack, K., & Clarke, A. B. (2019). H 2 O–CO 2 solubility in alkali-rich mafic magmas: new experiments at mid-crustal pressures. *Contributions to Mineralogy and Petrology*, *174*(7), 1–24.

Allison, C. M., Roggensack, K., & Clarke, A. B. (2021). Highly explosive basaltic eruptions driven by CO2 exsolution. *Nature Communications*, *12*(1), 1–10. https://doi.org/10.1038/s41467-020-20354-2

Allison, C. M., Roggensack, K., & Clarke, A. B. (2022). MafiCH: a general model for H2O–CO2 solubility in mafic magmas. *Contributions to Mineralogy and Petrology*, *177*(3), 1–22. https://doi.org/10.1007/s00410-022-01903-y

Ammannati, E., Jacob, D. E., Avanzinelli, R., Foley, S. F., & Conticelli, S. (2016). Low Ni olivine in silica-undersaturated ultrapotassic igneous rocks as evidence for carbonate metasomatism in the mantle. *Earth and Planetary Science Letters*, *444*, 64–74. https://doi.org/10.1016/j.epsl.2016.03.039

Anderson, A. T. (1995). CO2 and the eruptibility of picrite and komatiite. *Lithos*, *34*(1–3), 19–25.

Anderson JR, A. T. (1974). Evidence for a picritic, volatile-rich magma beneath Mt. Shasta, California. *Journal of Petrology*, *15*(2), 243–267.

Bamber, E. C., Arzilli, F., Polacci, M., Hartley, M. E., Fellowes, J., Di Genova, D., Chavarría, D., Saballos, J. A., & Burton, M. R. (2020). Pre-and syn-eruptive conditions of a basaltic Plinian eruption at Masaya Volcano, Nicaragua: the Masaya Triple Layer (2.1 ka). *Journal of Volcanology and Geothermal Research*, *392*, 106761.

Barth, A., Newcombe, M., Plank, T., Gonnermann, H., Hajimirza, S., Soto, G. J., Saballos, A., & Hauri, E. (2019). Magma decompression rate correlates with explosivity at basaltic volcanoes—Constraints from water diffusion in olivine. *Journal of Volcanology and Geothermal Research*, *387*, 106664.

Barth, A., Plank, T., & Towbin, H. (2023). Rates of dehydration in hydrous, high-Fo, magmatic olivines. *Geochimica et Cosmochimica Acta*, *342*, 62–73.

Branca, S., & Del Carlo, P. (2005). Types of eruptions of Etna volcano AD 1670–2003: implications for short-term eruptive behaviour. *Bulletin of Volcanology*, *67*(8), 732–742.

Carnevale, G., Caracausi, A., Rotolo, S. G., Paternoster, M., & Zanon, V. (2022). New Inferences on Magma Dynamics in Melilitite-Carbonatite Volcanoes: The Case Study of Mt. Vulture (Southern Italy). *Geophysical Research Letters*, *49*(21). https://doi.org/10.1029/2022GL099075

Cassidy, M., Manga, M., Cashman, K., & Bachmann, O. (2018). Controls on explosive-effusive volcanic eruption styles. *Nature Communications*, *9*(1). https://doi.org/10.1038/s41467-018-05293-3

Coltelli, M., Del Carlo, P., Pompilio, M., & Vezzoli, L. (2005). Explosive eruption of a picrite: The 3930 BP subplinian eruption of Etna volcano (Italy). *Geophysical Research Letters*, *32*(23), 1–4. https://doi.org/10.1029/2005GL024271

Coltelli, M., Del Carlo, P., & Vezzoli, L. (1998). Discovery of a Plinian basaltic eruption of Roman age at Etna volcano, Italy. *Geology*, *26*(12), 1095–1098. https://doi.org/10.1130/0091-7613(1998)026<1095:DOAPBE>2.3.CO;2

Coltelli, M., Del Carlo, P., & Vezzoli, L. (2000). Stratigraphic constraints for explosive activity in the past 100 ka at Etna Volcano, Italy. *International Journal of Earth Sciences*, *89*(3), 665–677. https://doi.org/10.1007/s005310000117

Correale, A., Paonita, A., Martelli, M., Rizzo, A., Rotolo, S. G., Anna, R., & Di, V. (2014). Lithos A two-component mantle source feeding Mt . Etna magmatism : Insights from the geochemistry of primitive magmas. *LITHOS*, *184–187*, 243–258. https://doi.org/10.1016/j.lithos.2013.10.038

Corsaro, R. A., Andronico, D., Behncke, B., Branca, S., Caltabiano, T., Ciancitto, F., Cristaldi, A., De Beni, E., La Spina, A., Lodato, L., Miraglia, L., Neri, M., Salerno, G., Scollo, S., & Spata, G. (2017). Monitoring the December 2015 summit eruptions of Mt. Etna (Italy): Implications on eruptive dynamics. *Journal of Volcanology and Geothermal Research*, *341*(December 2015), 53–69. https://doi.org/10.1016/j.jvolgeores.2017.04.018

Corsaro, R. A., & Métrich, N. (2016). Chemical heterogeneity of Mt. Etna magmas in the last 15 ka. Inferences on their mantle sources. *Lithos*, *252–253*, 123–134. https://doi.org/10.1016/j.lithos.2016.02.006

Corsaro, R. A., & Pompilio, M. (2004). Buoyancy-controlled eruption of magmas at Mt Etna. *Terra Nova*, *16*(1), 16–22.

Currenti, G., Del Negro, C., & Ganci, G. (2007). Modelling of ground deformation and gravity fields using finite element method: An application to Etna volcano. *Geophysical Journal International*, *169*(2), 775–786. https://doi.org/10.1111/j.1365-246X.2007.03380.x

Danyushevsky, L. V, Leslie, R. A. J., Crawford, A. J., & Durance, P. (2004). Melt inclusions in primitive olivine phenocrysts: the role of localized reaction processes in the origin of anomalous compositions. *Journal of Petrology*, *45*(12), 2531–2553.

Dasgupta, R., Hirschmann, M. M., & Smith, N. D. (2007). Partial melting experiments of peridotite+ CO2 at 3 GPa and genesis of alkalic ocean island basalts. *Journal of Petrology*, *48*(11), 2093–2124.

Davis, T., Rivalta, E., Smittarello, D., & Katz, R. F. (2023). Ascent rates of 3-D fractures driven by a finite batch of buoyant fluid. *Journal of Fluid Mechanics*, *954*, 1–23. https://doi.org/10.1017/jfm.2022.986

Dellong, D., Klingelhoefer, F., Kopp, H., Graindorge, D., Margheriti, L., Moretti, M., Murphy, S., & Gutscher, M. A. (2018). Crustal Structure of the Ionian Basin and Eastern Sicily Margin: Results From a Wide-Angle Seismic Survey. *Journal of Geophysical Research: Solid Earth*, *123*(3), 2090–2114. https://doi.org/10.1002/2017JB015312

Di Genova, D., Romano, C., Alletti, M., Misiti, V., & Scarlato, P. (2014). The effect of CO2 and H2O on Etna and Fondo Riccio (Phlegrean Fields) liquid viscosity, glass transition temperature and heat capacity. *Chemical Geology*, *377*, 72–86.

Ding, S., Plank, T., Wallace, P. J., & Rasmussen, D. J. (2023). Sulfur_X: A model of sulfur degassing during magma ascent. *Geochemistry, Geophysics, Geosystems*, *24*(4), e2022GC010552.

Dixon, J. E. (1997). Degassing of alkalic basalts. *American Mineralogist*, *82*(3–4), 368–378.

Dixon, J. E., Leist, L., Langmuir, C., & Schilling, J.-G. (2002). Recycled dehydrated lithosphere observed in plume-influenced mid-ocean-ridge basalt. *Nature*, *420*(6914), 385–389. https://doi.org/10.1038/nature01215

Dohmen, R., & Chakraborty, S. (2007). Fe-Mg diffusion in olivine II: Point defect chemistry, change of diffusion mechanisms and a model for calculation of diffusion coefficients in natural olivine. *Physics and Chemistry of Minerals*, *34*(6), 409–430. https://doi.org/10.1007/s00269-007-0158-6

Duan, X. (2014). A general model for predicting the solubility behavior of H2O–CO2 fluids in silicate melts over a wide range of pressure, temperature and compositions. *Geochimica et Cosmochimica Acta*, *125*, 582–609.

Esposito, R., Lamadrid, H. M., Redi, D., Steele-MacInnis, M., Bodnar, R. J., Manning, C. E.,

De Vivo, B., Cannatelli, C., & Lima, A. (2016). Detection of liquid H2O in vapor bubbles in reheated melt inclusions: Implications for magmatic fluid composition and volatile budgets of magmas? *American Mineralogist*, *101*(7), 1691–1695.
Gennaro, E., Grassa, F., Martelli, M., Renzulli, A., & Rizzo, A. L. (2017). Carbon isotope composition of CO2-rich inclusions in cumulate-forming mantle minerals from Stromboli volcano (Italy). *Journal of Volcanology and Geothermal Research*, *346*, 95–103. https://doi.org/https://doi.org/10.1016/j.jvolgeores.2017.04.001
Gennaro, E., Iacono-Marziano, G., Paonita, A., Rotolo, S. G., Martel, C., Rizzo, A. L., Pichavant, M., & Liotta, M. (2019). Melt inclusions track melt evolution and degassing of Etnean magmas in the last 15 ka. *Lithos*, *324–325*, 716–732. https://doi.org/10.1016/j.lithos.2018.11.023
Gennaro, E., Paonita, A., Iacono-Marziano, G., Moussallam, Y., Pichavant, M., Peters, N., & Martel, C. (2020). Sulphur behaviour and redox conditions in etnean magmas during magma differentiation and degassing. *Journal of Petrology*. https://doi.org/10.1093/petrology/egaa095
Ghiorso, M. S., & Gualda, G. A. R. (2015). An H 2 O–CO 2 mixed fluid saturation model compatible with rhyolite-MELTS. *Contributions to Mineralogy and Petrology*, *169*(6), 1–30.
Giordano, D., & Dingwell, D. (2003). Viscosity of hydrous Etna basalt: implications for Plinian-style basaltic eruptions. *Bulletin of Volcanology*, *65*(1), 8–14. https://doi.org/10.1007/s00445-002-0233-2
Giordano, D., Russell, J. K., & Dingwell, D. B. (2008). Viscosity of magmatic liquids: A model. *Earth and Planetary Science Letters*, *271*(1–4), 123–134. https://doi.org/10.1016/j.epsl.2008.03.038
Giuffrida, M., Viccaro, M., & Ottolini, L. (2018). Ultrafast syn-eruptive degassing and ascent trigger high-energy basic eruptions. *Scientific Reports*, *8*(1), 1–7. https://doi.org/10.1038/s41598-017-18580-8
Gvirtzman, Z., & Nur, A. (1999). The formation of Mount Etna as the consequence of slab rollback. *Nature*, *401*(6755), 782–785. https://doi.org/10.1038/44555
Houghton, B. F., & Gonnermann, H. M. (2008). Basaltic explosive volcanism: Constraints from deposits and models. *Chemie Der Erde - Geochemistry*, *68*(2), 117–140. https://doi.org/http://dx.doi.org/10.1016/j.chemer.2008.04.002
Houghton, B. F., Wilson, C. J. N., Del Carlo, P., Coltelli, M., Sable, J. E., & Carey, R. (2004). The influence of conduit processes on changes in style of basaltic Plinian eruptions: Tarawera 1886 and Etna 122 BC. *Journal of Volcanology and Geothermal Research*, *137*(1-3 SPEC. ISS.), 1–14. https://doi.org/10.1016/j.jvolgeores.2004.05.009
Iacono-Marziano, G., Morizet, Y., Le Trong, E., & Gaillard, F. (2012). New experimental data and semi-empirical parameterization of H2O–CO2 solubility in mafic melts. *Geochimica et Cosmochimica Acta*, *97*, 1–23.
Iacovino, K., Matthews, S., Wieser, P. E., Moore, G. M., & Bégué, F. (2021). VESIcal Part I: An open-source thermodynamic model engine for mixed volatile (H2O-CO2) solubility in silicate melts. *Earth and Space Science*, *8*(11), e2020EA001584.
Kamenetsky, V., & Clocchiatti, R. (1996). Primitive magmatism of Mt. Etna: Insights from mineralogy and melt inclusions. *Earth and Planetary Science Letters*, *142*(3–4), 553–572. https://doi.org/10.1016/0012-821x(96)00115-x
Kamenetsky, V., Pompilio, M., Métrich, N., Sobolev, A. V., Kuzmin, D. V., & Thomas, R. (2007). Arrival of extremely volatile-rich high-Mg magmas changes explosivity of Mount Etna. *Geology*, *35*(3), 255–258. https://doi.org/10.1130/G23163A.1
Lara, M., & Dasgupta, R. (2022). Carbon recycling efficiency in subduction zones constrained by the effects of H2O-CO2 fluids on partial melt compositions in the mantle

wedge. *Earth and Planetary Science Letters*, *588*. https://doi.org/10.1016/j.epsl.2022.117578

Lerner, A. H., Muth, M. J., Wallace, P. J., Lanzirotti, A., Newville, M., Gaetani, G. A., Chowdhury, P., & Dasgupta, R. (2021). Improving the reliability of Fe- and S-XANES measurements in silicate glasses: Correcting beam damage and identifying Fe-oxide nanolites in hydrous and anhydrous melt inclusions. *Chemical Geology*, *586*, 120610. https://doi.org/https://doi.org/10.1016/j.chemgeo.2021.120610

McPhie, J., Walker, G. P. L., & Christiansen, R. L. (1990). Phreatomagmatic and phreatic fall and surge deposits from explosions at Kilauea volcano, Hawaii, 1790 AD: Keanakakoi Ash Member. *Bulletin of Volcanology*, *52*, 334–354.

Mironov, N., Portnyagin, M., Botcharnikov, R., Gurenko, A., Hoernle, K., & Holtz, F. (2015). Quantification of the CO2 budget and H2O-CO2 systematics in subduction-zone magmas through the experimental hydration of melt inclusions in olivine at high H2O pressure. *Earth and Planetary Science Letters*, *425*, 1–11. https://doi.org/10.1016/j.epsl.2015.05.043

Moore, L. R., Gazel, E., Tuohy, R., Lloyd, A. S., Esposito, R., Steele-MacInnis, M., Hauri, E. H., Wallace, P. J., Plank, T., & Bodnar, R. J. (2015). Bubbles matter: An assessment of the contribution of vapor bubbles to melt inclusion volatile budgets. *American Mineralogist*, *100*(4), 806–823. https://doi.org/10.2138/am-2015-5036

Moussallam, Y., Médard, E., Georgeais, G., Rose-Koga, E. F., Koga, K. T., Pelletier, B., Bani, P., Shreve, T. L., Grandin, R., Boichu, M., Tari, D., & Peters, N. (2021). How to turn off a lava lake? A petrological investigation of the 2018 intra-caldera and submarine eruptions of Ambrym volcano. *Bulletin of Volcanology*, *83*(5), 36. https://doi.org/10.1007/s00445-021-01455-2

Moussallam, Y., Rose-Koga, E. F., Koga, K. T., Médard, E., Bani, P., Devidal, J.-L., & Tari, D. (2019). Fast ascent rate during the 2017–2018 Plinian eruption of Ambae (Aoba) volcano: a petrological investigation. *Contributions to Mineralogy and Petrology*, *174*(11), 90. https://doi.org/10.1007/s00410-019-1625-z

Mutch, E. J. F., Maclennan, J., Shorttle, O., Edmonds, M., & Rudge, J. F. (2019). Rapid transcrustal magma movement under Iceland. *Nature Geoscience*, *12*(7), 569–574.

Mutch, E. J. F., Maclennan, J., Shorttle, O., Rudge, J. F., & Neave, D. A. (2021). DFENS: Diffusion chronometry using finite elements and nested sampling. *Geochemistry, Geophysics, Geosystems*, *22*(4), e2020GC009303.

Namiki, A., & Manga, M. (2006). Influence of decompression rate on the expansion velocity and expansion style of bubbly fluids. *Journal of Geophysical Research: Solid Earth*, *111*(11), 1–17. https://doi.org/10.1029/2005JB004132

Newcombe, M. E., Plank, T., Barth, A., Asimow, P., & Hauri, E. (2020). Water-in-olivine magma ascent chronometry: Every crystal is a clock. *Journal of Volcanology and Geothermal Research*, 106872.

Nicolich, R., Laigle, M., Hirn, A., Cernobori, L., & Gallart, J. (2000). Crustal structure of the ionian margin of Sicily: Etna volcano in the frame of regional evolution. *Tectonophysics*, *329*(1–4), 121–139. https://doi.org/10.1016/S0040-1951(00)00192-X

Parfitt, E. A., & Wilson, L. (1994). Modelling the transition between Hawaiin-style lava fountaining and Strombolian explosive volcanic activity. *Abstracts of the 25th Lunar and Planetary Science Conference*, *1 995*, 1049–1050. http://adsabs.harvard.edu/full/1994LPI....25.1049P

Pichavant, M., Di Carlo, I., Rotolo, S. G., Scaillet, B., Burgisser, A., Le Gall, N., & Martel, C. (2013). Generation of CO2-rich melts during basalt magma ascent and degassing. *Contributions to Mineralogy and Petrology*, *166*(2), 545–561. https://doi.org/10.1007/s00410-013-0890-5

Portnyagin, M., Hoernle, K., Plechov, P., Mironov, N., & Khubunaya, S. (2007). Constraints on mantle melting and composition and nature of slab components in volcanic arcs from volatiles (H2O, S, Cl, F) and trace elements in melt inclusions from the Kamchatka Arc. *Earth and Planetary Science Letters*, *255*(1–2), 53–69.

Portnyagin, M. V, Mironov, N. L., Matveev, S. V, & Plechov, P. Y. (2005). Petrology of avachites, high-magnesian basalts of Avachinsky Volcano, Kamchatka: II. Melt inclusions in olivine. *PETROLOGY C/C OF PETROLOGIIA*, *13*(4), 322.

Qin, Z., Lu, F., & Anderson, A. T. (1992). Diffusive reequilibration of melt and fluid inclusions. *American Mineralogist*, *77*(5–6), 565–576.

Rasmussen, D. J., Plank, T. A., Wallace, P. J., Newcombe, M. E., & Lowenstern, J. B. (2020). Vapor-bubble growth in olivine-hosted melt inclusions. *American Mineralogist*, *105*(12), 1898–1919.

Reed, M. H., Munoz-Saez, C., Hajimirza, S., Wu, S.-M., Barth, A., Girona, T., Rasht-Behesht, M., White, E. B., Karplus, M. S., & Hurwitz, S. (2021). The 2018 reawakening and eruption dynamics of Steamboat Geyser, the world's tallest active geyser. *Proceedings of the National Academy of Sciences*, *118*(2).

Ruprecht, P., & Plank, T. (2013). Feeding andesitic eruptions with a high-speed connection from the mantle. *Nature*, *500*(7460), 68–72.

Schiano, P., Clocchiatti, R., Ottolini, L., & Busà, T. (2001). Transition of Mount Etna lavas from a mantle-plume to an island-arc magmatic source [6]. *Nature*, *412*(6850), 900–904. https://doi.org/10.1038/35091056

Schiano, P., Eiler, J. M., Hutcheon, I. D., & Stolper, E. M. (2000). Primitive CaO-rich, silica-undersaturated melts in island arcs: Evidence for the involvement of clinopyroxene-rich lithologies in the petrogenesis of arc magmas. *Geochemistry, Geophysics, Geosystems*, *1*(5). https://doi.org/10.1029/1999gc000032

Shea, T., Ruth, D., Jollands, M., Ohtaki, K., Ishii, H., & Bradley, J. (2023). The presence of silicate melt may enhance rates of cation diffusion in olivine. *Earth and Planetary Science Letters*, *621*, 118370. https://doi.org/10.1016/j.epsl.2023.118370

Spandler, C., & O'Neill, H. S. C. (2010). Diffusion and partition coefficients of minor and trace elements in San Carlos olivine at 1,300 C with some geochemical implications. *Contributions to Mineralogy and Petrology*, *159*, 791–818.

Steele-MacInnis, M., Esposito, R., Moore, L. R., & Hartley, M. E. (2017). Heterogeneously entrapped, vapor-rich melt inclusions record pre-eruptive magmatic volatile contents. *Contributions to Mineralogy and Petrology*, *172*(4), 1–13. https://doi.org/10.1007/s00410-017-1343-3

Tonarini, S., Armienti, P., D'Orazio, M., & Innocenti, F. (2001). Subduction-like fluids in the genesis of Mt. Etna magmas: evidence from boron isotopes and fluid mobile elements. *Earth and Planetary Science Letters*, *192*(4), 471–483.

Tonarini, S., D'Orazio, M., Armienti, P., Innocenti, F., & Scribano, V. (1996). Geochemical features of eastern Sicily lithosphere as probed by Hyblean xenoliths and lavas. *European Journal of Mineralogy*, *8*(5), 1153–1173.

Toplis, M. J. (2005). The thermodynamics of iron and magnesium partitioning between olivine and liquid: Criteria for assessing and predicting equilibrium in natural and experimental systems. *Contributions to Mineralogy and Petrology*, *149*(1), 22–39. https://doi.org/10.1007/s00410-004-0629-4

Trua, T., Esperança, S., & Mazzuoli, R. (1998). The evolution of the lithospheric mantle along the N. African Plate: Geochemical and isotopic evidence from the tholeiitic and alkaline volcanic rocks of the Hyblean plateau, Italy. *Contributions to Mineralogy and Petrology*, *131*(4), 307–322. https://doi.org/10.1007/s004100050395

Turner, S. J., & Langmuir, C. H. (2015). The global chemical systematics of arc front

stratovolcanoes: Evaluating the role of crustal processes. *Earth and Planetary Science Letters*, *422*, 182–193.

Viccaro, M., & Cristofolini, R. (2008). Nature of mantle heterogeneity and its role in the short-term geochemical and volcanological evolution of Mt. Etna (Italy). *Lithos*, *105*(3–4), 272–288. https://doi.org/10.1016/j.lithos.2008.05.001

Wallace, P. J., Plank, T., Bodnar, R. J., Gaetani, G. A., & Shea, T. (2021). Olivine-Hosted Melt Inclusions: A Microscopic Perspective on a Complex Magmatic World. *Annual Review of Earth and Planetary Sciences*, *49*.

Walter, M. J. (1998). Melting of garnet peridotite and the origin of komatiite and depleted lithosphere. *Journal of Petrology*, *39*(1), 29–60.

Zuccarello, F., Schiavi, F., & Viccaro, M. (2022). The eruption run-up at Mt. Etna volcano: Constraining magma decompression rates and their relationships with the final eruptive energy. *Earth and Planetary Science Letters*, *597*, 117821. https://doi.org/10.1016/j.epsl.2022.117821

Declaration of interests

☒ The authors declare that they have no known competing financial interests or personal relationships that could have appeared to influence the work reported in this paper.

☐ The author is an Editorial Board Member/Editor-in-Chief/Associate Editor/Guest Editor for *[Journal name]* and was not involved in the editorial review or the decision to publish this article.

☐ The authors declare the following financial interests/personal relationships which may be considered as potential competing interests: